

Performance mutation mechanism and parametric characterization method of high-capacity lithium-ion battery

Yubin Wang¹, Caiping Zhang^{1*}, Linjing Zhang¹, Xiaohong Li², Sijia Yang¹, Xinyu Jia¹

¹ National Active Distribution Network Technology Research Center (NANTEC), Beijing Jiaotong

University, Beijing 100044, China

² Renewable Energy Group, College of Engineering, Mathematics and Physical Sciences, University of

Exeter, Penryn Campus, Cornwall, TR10 9FE, United Kingdom

Abstract

The mutation of power battery performance brings serious reliability and safety problems, and has developed into an urgent common issue of electric vehicle power battery running and echelon utilization. It is essential to investigate the performance mutation mechanism and parametric characterization method of lithium-ion batteries. In this paper, the mutation effect of battery performance under state of charge (SOC) interval and temperature cyclic conditions is discovered. Moreover, thermodynamic investigation method based on the half-cell potential synthesis is implemented to explore the evolution of equilibrium potential. Furthermore, the dynamic investigation method based on distribution of relaxation time (DRT) and equivalent circuit model (ECM) are introduced to describe the impedance characteristics of batteries. Eventually, the mechanism of battery performance mutation is revealed and the parameters characterizing the mutation are extracted. The mutation effect contains inducing point and crossing point, and is caused by the mutation of the negative active material. In addition, the charge transfer impedance and diffusion impedance in the SOC range of 10%-20% are particularly sensitive to the mutation, and a feasible method for identifying mutant battery and aging path based on the extracted parameters is proposed. It provides superintendence for the safe and economical application of power batteries.

Keywords: Performance mutation; Thermodynamic investigation; Dynamic investigation; Distribution of relaxation time; Parametric characterization

1 Introduction

The transition to electric vehicles (EVs) is set to accelerate over this coming decades as governments and legislatures around the world are increasingly committed to the electrification of road transport. Currently, the stock of EVs is rapidly soaring, and the large-scale adoption of EVs has contributed to the boom in power batteries [1]. However, though the mileage range of EVs is increasing impressively, the performance degradation of battery is always inevitable, which poses two challenges to be overcome, the safe running and recycling of EVs power batteries [2, 3].

It is often expected that the battery capacity degradation can be maintained at a steady level when subjecting to the increase of cycles number in the process of normal performance degradation [4]. We have conducted routine cycle aging tests on hundreds of commercial ternary lithium-ion batteries from two different manufacturers, and unexpectedly found that 50% of them experienced performance mutation[5]. Furthermore, when most batteries reach the knee point of the battery performance, the capacity retention rate is still greater than 90%. It is far from the decommissioning conditions of the EVs power batteries. Meanwhile, the performance mutation is accompanied by a significant expansion in size. It is a major hidden danger for the safe running of the battery system, in very unfortunate circumstances, it can result in a fire and explosion of the battery. In addition, when the batteries retire from EVs, if the performance mutation occurs, it may even have a negative impact on the echelon utilization of the batteries. It can be seen that the performance mutation is the common issue of EVs power battery operation running and echelon utilization.

The research on lithium-ion battery performance mutation is now mainly focused on the mechanism, modeling and prediction methods.

The exploration of the mechanism relies on qualitative analysis through post-dismantling [6-12]. It is revealed that the uneven distribution of the internal pressure of the battery [7] and the lithium deposition at the interface between the negative electrode

and the separator [9, 10] are responsible for the mutation. For example, Bacha et al. [7] reported that the unevenness of the pressure inside the battery in actual use leads to uneven current distribution, thereby causing the performance mutation of batteries. Sarasketa et al. [9] discovered that the capacity loss of the battery is aroused by the growth of the solid electrolyte interface (SEI) layer, leading to local lithium deposition. While most existing literature of degradation mechanism have been emphasized on lithium deposition [13], the effects of electrode active material loss and electrode dynamics loss on performance mutation have not been discussed in depth, and quantitative descriptions of the mutation mechanisms are even less available.

There exists conventionally a considerable number of performance degradation modeling methods for batteries including empirical models [14-17, 28], equivalent circuit models [18, 19], impedance models [20-22] and electrochemical models [23, 24]. Model parameters are determined by training a large amount of test data from the laboratory. However, due to the limitation of training data, especially when there is a significant difference between training conditions and actual conditions, the applicability of this method can be in question mark. For example, if the training data set contains only conditions for a steady degradation in battery performance, once the mutation occurs, the prediction of the model will be invalid. Pseudo two-dimensional (P2D) models [23], single particle (SP) models [25], and electrochemical models with degraded physical properties [26] have also been established to simulate the internal and external characteristics of battery performance mutation. The obvious obstacle is that due to the manufacturer's confidentiality measures and the coupling of multiple parameters, accurate parameter acquisition and identification are very difficult.

The prediction of the knee point of the battery performance is generally based on data threshold [27] and probability derived from statistical methods [5]. It is dominated by personal will that apply threshold to identify the knee point of the battery performance. Maheshwari et al. [27] presumed that the criterion of the knee point is that the local rate of capacity degradation exceeds more than twice the overall rate. Moreover, the rate calculation should be performed every 100 equivalent full cycles

(EFC) to avoid capacity fluctuations caused by capacity recovery effects and/or possible error of data measurement, which may cause the identification results to lag seriously. Some researchers have expanded battery capacity prediction and health state estimation methods [28-30]. Among them, Cong et al. [30] initially predicted the battery capacity, and then determined that the first-order derivative of the battery capacity exceeded the 3σ threshold range to achieve the purpose of identifying the knee point of battery performance. The above method considers only the features of capacity data. However, since the actual capacity is difficult to obtain accurately, its application is limited. Compared with the prediction method based on the battery degradation mechanism, the guiding significance is weakened.

As indicated, the current research has highlighted that the core problem is that the mechanism of mutation and the characterization of related physical parameters are ambiguous. Therefore, this paper combines the half-cell model and impedance model to deeply explore their relationship with mutation in terms of battery positive/negative electrode capacity, available lithium-ion capacity, and positive and negative electrode kinetic parameters. The mechanism of battery performance mutation under different cycling conditions has been revealed. The foremost characterization parameters that induce performance mutation are extracted. It provides guidance for the prediction methods of performance mutation, and engenders considerable scientific value and practical implication for the safe and economical application of power batteries.

2 Experimental test matrix and performance mutation phenomenon

In this study, the battery selected in the experiment was a commercial ternary high-capacity lithium-ion battery with Nickel–Manganese–Cobalt (NMC) based positive and graphite based negative electrodes. The nominal capacity of the cell is 114 Ah, and the charge-discharge cut-off voltage is 2.8-4.25 V. By aiming to observe the evolution of battery performance degradation, the experimental program is divided into performance test and cycle test.

The performance test set includes rated capacity test, small current equilibrium potential test, and Electrochemical Impedance Spectroscopy (EIS) test. If not otherwise

stated, the test temperature is set to 25 °C. The acquisition of the rated capacity is carried out in accordance with the scheme provided in the battery manual, and the charging strategy adopts a step current charging method. A total of four different current rates are selected during the battery charging process. As the SOC increases, the current gradually decreases in the order of 1 C, 1/3 C, 1/10 C and 1/20 C, respectively. After being fully charged and standing for 6 minutes, the battery is discharged with a constant current of 1/3 C to the cut-off voltage of 2.8 V. The equilibrium potential is calculated by taking the mean of the charge and discharge voltage with constant current of 0.05 C. The EIS test of the battery is conducted sequentially at the decile of the battery SOC, and the voltage response of the battery does not exceed 10 mV to meet the requirements of its linearity and stability conditions. The frequency range from 10 kHz to 10 mHz is selected to obtain a complete and accurate impedance spectrum of the battery.

The cycle test is conducted under two working conditions, the influential factors considered are the temperature and SOC interval. The temperature range covers from 25 °C to 55 °C. The depth of discharge (DOD) for the SOC interval is 20%, and the mean of SOC is distributed on the low, medium and high levels of battery SOC namely, 10% SOC (M₁₀D₂₀), 50% SOC (M₅₀D₂₀) and 90% SOC (M₉₀D₂₀). The charging strategy of the cycle test is consistent with the rated capacity test in the corresponding SOC interval. The slight difference is that the discharge rate of the cycle test is 1 C, and when the discharge reaches the cut-off voltage, it needs to be further switched to 1/3 C and discharged to the cut-off voltage again.

To investigate the performance degradation of the battery under different temperatures and SOC intervals, the condition that the mean SOC is 50% and the DOD is 100% at 25 °C (25°C@M₅₀D₁₀₀) is used as a reference. During the experiment process, the basic performance test is performed after multiple cycles of the aging test. The detailed aging experiment matrix and declining state of battery are depicted in Table 1. To ensure the safety of the experiment and the consistency with the actual operating conditions, the batteries are tested with splints. The test equipment is American Arbin LBT21014 Battery Testing System and the experimental batteries are placed in a high and low temperature test chamber to keep the constant temperature. At least two

batteries are tested at the same condition, so as to avoid the contingency of the experiment.

Table. 1 Battery aging experiment matrix. The M_xD_y represents the condition of mean SOC x and DOD y . The ACC and Nor represent the accelerated and normal declining state of battery performance, respectively.

Considered condition	Temperature (°C)	SOC interval (Level)	Current rate Charge-Discharge (C)	Declining state
SOC interval	25	$M_{10}D_{20}$ (Low)	1-1&1/3	Acc
		$M_{50}D_{20}$ (Medial)	1-1	Nor
		$M_{90}D_{20}$ (High)	1/3&1/10&1/20-1	Nor
Reference	25	$M_{50}D_{100}$ (Full)	1&1/3 &1/10 &1/20 -1&1/3	Acc/Nor
		Temperature	35	$M_{50}D_{100}$ (Full)
45	1&1/3&1/10&1/20		Nor	
55	-1&1/3		Nor	

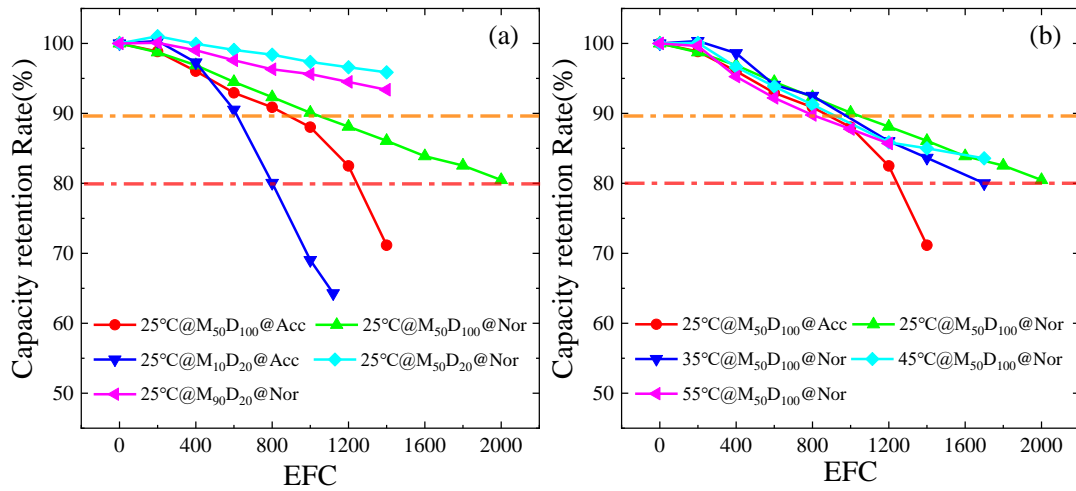


Fig. 1. Decay curve of battery capacity retention rate (a) Decline curve of capacity retention rate under different SOC interval cycle conditions (b) Decline curve of capacity retention rate under different temperature cycle conditions

The decay process of the rated capacity retention rate of the battery under various operating conditions is shown in Fig. 1. Due to the distinct difference in the number of

battery cycles under different operating conditions, especially in the case of partial SOC interval, the EFC is used to facilitate unification. The capacity decay process of several batteries under the same working condition remains coincident, except for the inconsistent battery decay trend of the batteries in the reference working condition ($25^{\circ}\text{C}@M_{50}D_{100}$). Thus, only one battery with the consistent degradation process is displayed. Under the condition of $25^{\circ}\text{C}@M_{50}D_{100}$, some batteries experienced accelerated capacity degradation, while other batteries still maintained approximately linear decline. In terms of SOC interval as illustrated in Fig. 1(a), the performance degradation of $25^{\circ}\text{C}@M_{50}D_{20}@Nor$, $25^{\circ}\text{C}@M_{90}D_{20}@Nor$ and $25^{\circ}\text{C}@M_{50}D_{100}@Nor$ meets the expected stability, and the degradation speed of $25^{\circ}\text{C}@M_{50}D_{100}@Nor$ is the highest. But the degradation speed of $25^{\circ}\text{C}@M_{10}D_{20}@Acc$ and $25^{\circ}\text{C}@M_{50}D_{100}@Acc$ is fast and a knee point appears. This phenomenon is defined as the performance mutation. Especially, the battery of $25^{\circ}\text{C}@M_{10}D_{20}@Acc$ appears a cliff-like drop as shown by blue curve in Fig. 1(a).

The performance mutation leads to a severe reduction in battery life. When declined to 80% of the rated capacity, the life span of $25^{\circ}\text{C}@M_{50}D_{100}@Nor$ is 2000 EFC. However, the battery life of $25^{\circ}\text{C}@M_{50}D_{100}@Acc$ is only about 1200 EFC, which is $3/5$ of the normal life. More seriously, for $25^{\circ}\text{C}@M_{10}D_{20}@Acc$, it begins to decline at an accelerated rate after 200 EFC, and the life is only $2/5$ of the normal life. This could be a terrible experience for customers. In term of temperature as illustrated in Fig. 1(b), as the temperature increases, the degradation rate of the battery capacity does not change evidently. A trend of approximately linear decline is presented without any mutation. It can be concluded that under normal temperature conditions, whether it is charged or discharged in a complete or partial SOC range, the battery is very likely to encounter the mutation in performance degradation. And lifting the battery ambient temperature, it will not remarkably reduce the battery life and cause battery performance mutation. Although the correlation between mutation and operating condition has been investigated, the cause of the mutation is confusing. Therefore, in order to better understand mechanism of battery performance degradation and identify

the knee point of performance, it is necessary to conduct in-depth investigation of the mutation mechanism and parametric characterization method.

3 Investigation of battery performance mutation

The manifestation of the battery performance is mainly determined by its equilibrium potential and impedance characteristics. Thence, it is necessary to start from its own properties of equilibrium potential and impedance to explore the evolution laws during the aging process, and to investigate the performance mutation mechanism. It is a potential method to synthesize the voltage of the whole battery based on the voltage curve of the positive and negative electrodes [31]. In the process of performance degradation, the contraction and translation characteristics of the voltage curve correspond to changes in capacity and impedance. It can further be utilized to determine the loss of positive electrode active material, negative electrode active material, available lithium ions and ohmic resistance during the decay process. Regretfully, the impedance of each part is lumped into an ohmic resistance, and the value is same in the entire SOC range. As a result, a significant error is caused and the inherent attenuation mechanism of each part impedance is hidden. Herein, based on the equilibrium potential of the half-cell, the equilibrium potential of the full-battery is accurately simulated, eliminating the error introduced by lumped resistance, and further takes advantage of the DRT and impedance model to reliably reflect the battery impedance features. Ultimately, the investigation methods of equilibrium potential and impedance characteristics are integrated to reveal the mutation mechanism of battery performance and to construct corresponding characteristic parameter set.

3.1 Mutation mechanism and parametric characterization method based on equilibrium potential

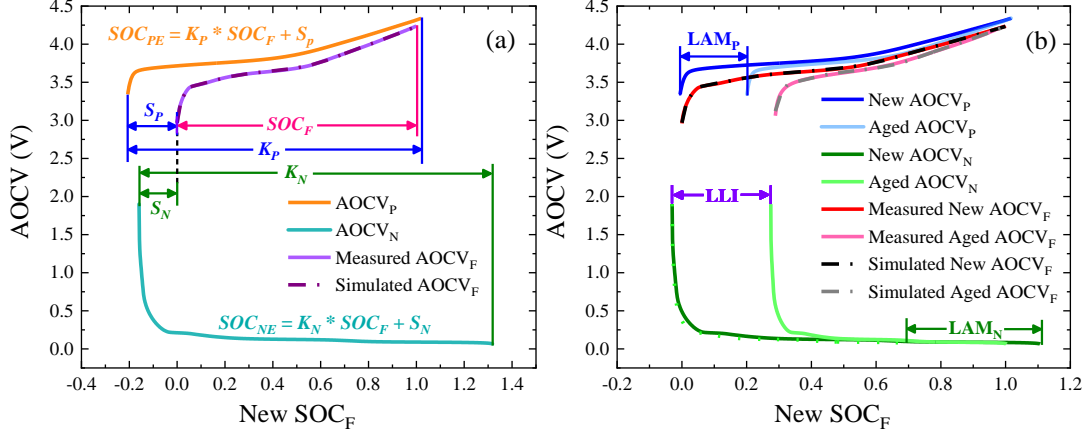


Fig. 2. Schematic diagram of battery approximate equilibrium potential synthesis method and the approximate equilibrium potential evolution after performance degradation (a) Schematic diagram of battery approximate equilibrium potential synthesis method (b) Evolution of approximate equilibrium potential after performance degradation

The credible acquisition of the cell equilibrium potential, also called the open circuit voltage (OCV), often requires several days of standing time, and thus is replaced by the approximate open circuit voltage (AOCV). Herein, for the positive half-cell, negative half-cell and full-battery, the voltage curves of charge and discharge at 0.05C are averaged to calculate AOCV. The low current and averaging strategy can extremely eliminate the influence of impedance on OCV. The AOCV of the positive electrode (AOCV_P), the AOCV of the negative electrode (AOCV_N) and the AOCV of the full-battery (AOCV_F) are illustrated in Fig. 2(a). As marked, K_P and K_N are contraction factors, and S_P and S_N are translation factors. SOC_{PE} , SOC_{NE} , and SOC_F are the SOC of the positive half-cell, negative half-cell, and full-battery, respectively. The AOCV_F of the new battery is calculated as follows:

$$AOCV_F = AOCV_P - AOCV_N = f(SOC_{PE}) - f(SOC_{NE}) \quad (1)$$

The loss of positive active material (LAM_P), the loss of negative active material (LAM_N), and the loss of available lithium ion (LLI) during the degradation of battery performance, resulting in the evolution of AOCV, as revealed in Fig. 2(b). Then the AOCV_F of the aging battery is calculated:

$$Aged AOCV_F = f(SOC_{PE}, LAM_P) - f(SOC_{NE}, LAM_N, LLI) \quad (2)$$

Simulate the relationship between the $AOCV_P$, $AOCV_N$ and the $AOCV_F$ at different stages of the battery life through the PSO optimization algorithm, so that the RMSE between the measured and simulated $AOCV_F$ is minimized. Thereby, the values of K_P , K_N , LAM_P , LAM_N , LLI can be determined. Furthermore, based on the correlation between the capacity of the new battery (Q_F) and specific parameters, the positive electrode material capacity (Q_P), negative electrode material capacity (Q_N) and available lithium-ion capacity (Q_{Li}) during the battery degradation are derived:

$$Q_x = \begin{cases} K_x * Q_F - LAM_x, & x = P, N \\ (K_P - S_P + S_N) * Q_F - LLI, & x = Li \end{cases} \quad (3)$$

The detailed introduction of the method can refer to our previous work[32]. In the light of fitting results of experimental lithium-ion batteries under different SOC intervals and different temperatures, the maximum error does not exceed 10 mV, and the model parameters are consistent. In addition, it has been verified on another battery that using a smaller charge and discharge current (0.02 C) to calculate the AOCV of the half-cell has a better fitting effect.

Fig. 3(a, b, c, d, e) display the variation curves of capacity during battery aging under different SOC interval cycle conditions. It can be clearly seen that the initial state of the battery under any operating condition satisfies: $Q_N > Q_{Li} > Q_P$. Since the decay trends of each capacity are not parallel, the decay rates of Q_F , Q_P , Q_N and Q_{Li} are inconsistent. The capacity decline trend of each part of the battery that has not experienced the performance mutation is relatively flat, and none of them exhibits a notable acceleration, as shown in Fig. 3(c, d, e). Under the operating conditions of $25^\circ\text{C}@M_{10}D_{20}@Acc$ and $25^\circ\text{C}@M_{50}D_{100}@Acc$ where the performance mutation occurs, the capacity degradation of each part is accelerated. In particular, the mutation of the negative electrode material capacity is the most significant, and the phenomena of induction and crossing is discovered in the mutation process, as shown in Fig. 3(a, b). Taking the operating condition of $25^\circ\text{C}@M_{10}D_{20}@Acc$ as an example. The degradation rate of each capacity is sluggish before 200 cycles. After that, the decay rate of Q_N suddenly accelerates, while the decay rate of Q_F , Q_P and Q_{Li} do not change appreciably. When Q_N decays below Q_P and Q_{Li} , Q_F , Q_P and Q_{Li} also begin to decline

faster. To facilitate description and understanding, the moment when Q_N suddenly drops is defined as the mutation inducing point (the point inside the yellow circle in Fig. 3(a)), and the moment when Q_N intersects with Q_P or Q_{Li} is defined as the mutation crossing point (the point inside the red circle in Fig. 3(a)). Identical behavior is derived under $25^\circ\text{C}@M_{10}D_{20}@Acc$ working condition, so it can be considered that the accelerated degradation of battery performance is mainly caused by the mutation of the negative electrode material. Thus, the whole mutation process can be characterized by the load rate (LR):

$$LR = \frac{Q_N}{Q_P} \quad (4)$$

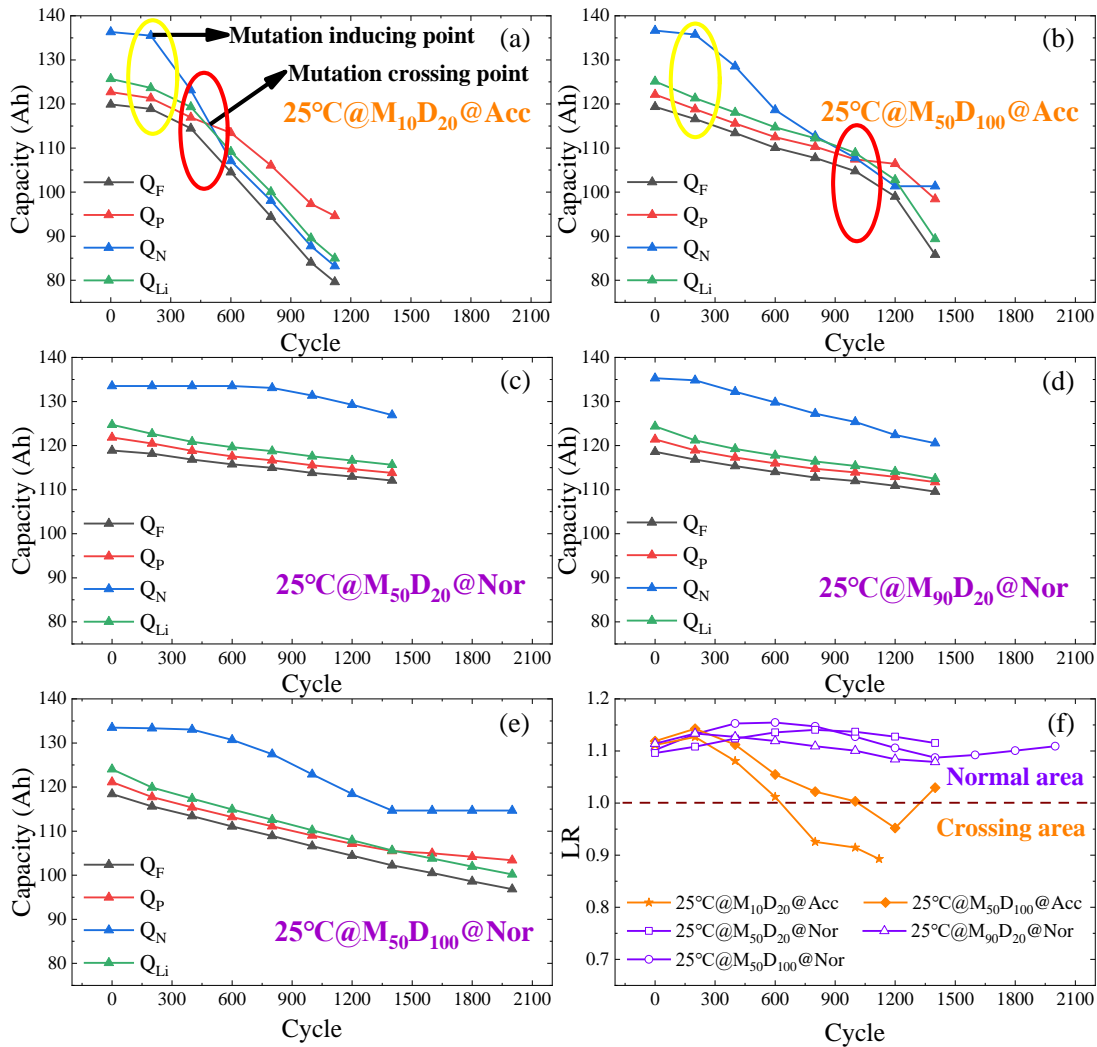


Fig. 3. The variation curves of each capacity and LR during battery aging under different SOC interval cycle conditions (a) The variation curve of each capacity at $25^\circ\text{C}@M_{10}D_{20}@Acc$ (b) The variation curve of each capacity at $25^\circ\text{C}@M_{50}D_{100}@Acc$ (c) The variation curve of each capacity

at 25°C@M₅₀D₂₀@Nor (d) The variation curve of each capacity at 25°C@M₉₀D₂₀@Nor (e) The variation curve of each capacity at 25°C@M₅₀D₁₀₀@Nor (f) The variation curve of LR under different SOC interval cycle conditions

The variation curve of LR under different SOC interval cycle conditions is represented in Fig. 3(f). Taking LR=1 as the boundary, the battery aging process is divided into normal area and crossing area. In the initial stage of battery aging, LR is >1. If there is no accelerated performance degradation, LR will always be in the normal degradation area of the battery. Once the LR exceeds the boundary and enters the crossing area, it indicates that the decay rate of the negative electrode material is markedly faster than the decay rate of the positive electrode material, and the battery performance exhibits the mutation.

The above-mentioned thermodynamic analysis method is also applied to different temperature cycle conditions. Corresponding variation curves of each capacity and LR are expressed in Fig. 4(a, b, c, d). The degradation of battery performance does not abruptly accelerate with the increase of cycle temperature ($T > 25\text{ }^{\circ}\text{C}$). However, LR reaches the boundary and enters the crossing area under the conditions of 35°C@M₅₀D₁₀₀@Nor and 45°C@M₅₀D₁₀₀@Nor, as shown in Fig. 4(d). Although the representation of LR is similar with the conditions of 25°C@M₅₀D₁₀₀@Acc and 25°C@M₁₀D₂₀@Acc, the variation curve of each capacity is diverse. Under the operating conditions of 35°C@M₅₀D₁₀₀@Nor and 45°C@M₅₀D₁₀₀@Nor, as shown in Fig. 4(a, b), when the negative electrode material decays to the mutation crossing point, its degradation rate begins to decrease, but it still accelerates at 25°C@M₁₀D₂₀@Acc (Fig. 3(a)). In addition, apart from the difference in negative electrode materials, the capacity of other parts does not accelerate decay in Fig. 4(a, b), but declines rapidly at 25°C@M₅₀D₁₀₀@Acc (Fig. 3(b)). When the temperature improves to 55 °C, as shown in Fig. 4(c), the mutation crossing point does not exist. Hence, the elevation of temperature is not the dominant factor that leads to the mutation of battery performance degradation.

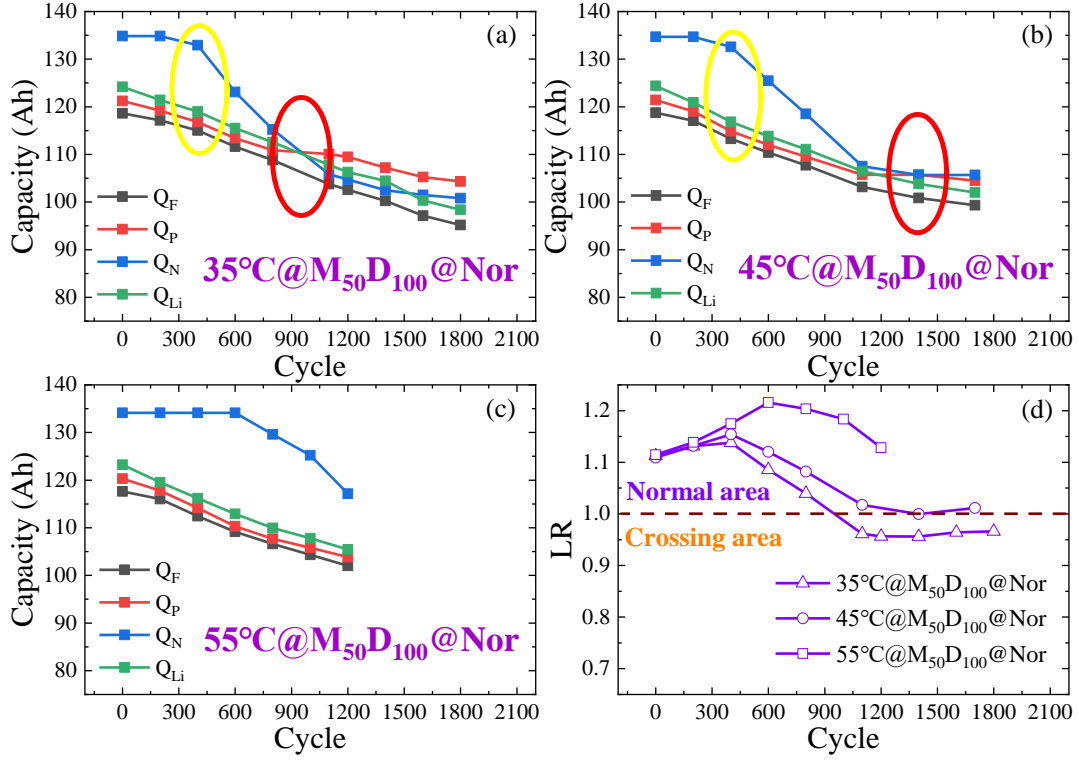


Fig. 4. The variation curves of each capacity and LR during battery aging under different temperature cycle conditions (a) The variation curve of each capacity at 35°C@M₅₀D₁₀₀@Nor (b) The variation curve of each capacity at 45°C@M₅₀D₁₀₀@Nor (c) The variation curve of each capacity at 55°C@M₅₀D₁₀₀@Nor (d) The variation curve of LR under different temperature cycle conditions

As stated previously, the analysis of the battery equilibrium potential under different cycle conditions confirms that the battery with performance mutation enters the intersection area during the aging process. But the battery that enters the intersection area does not necessarily have mutation. Only after entering the crossing area, the degradation of any material is still accelerated, which will lead to mutation of the battery performance. That is, the sufficient condition for the mutation of battery performance degradation is that the capacity ratio of the positive and negative active materials reverses, and the accelerated degradation of any material after the reversal is a necessary and sufficient condition. Hereby, the thermodynamic characteristic parameter θ_{TCP} can be extracted.

$$\theta_{TCP} = \{Q_P, Q_N, Q_{Li}, LR\} \quad (5)$$

The mutation mechanism and parametric characterization based on equilibrium potential is realized through θ_{TCP} . To further explore the dynamic characteristic parameters related to the mutation, the battery impedance feature and its model research are carried out.

3.2 Mutation mechanism and parameterized characterization based on impedance feature

The EIS testing equipment employed is the French Bio-Logic VMP-300 multi-channel electrochemical workstation. In order to extract the correct information from the impedance spectrum, the linearity, time invariance, and causality conditions must be satisfied. Lin-KK software based on Kramers-Kronig technology has been used to verify the reliability of all impedance spectroscopy experimental data [33]. According to the test results, a typical lithium-ion battery impedance spectrum is exhibited in Fig. 5(a). If ignoring the inductive impedance part below the real axis generated by wire inductance and electrode winding, the impedance spectrum is mainly composed of four parts: 1) The intersection with the real axis is the ohmic resistance of the battery, including the resistance of the solution and the electrode. 2) That located in the high frequency region is a small capacitive reactance arc which represents the migration process of lithium ions in the SEI film. 3) There is an incomplete large capacitive reactance arc in the intermediate frequency region, indicating the charge transfer process of lithium ions at the interface of the SEI film and the electrode active material. 4) An approximate straight line characterizing the diffusion process of lithium ions in the solid phase extends in the low frequency region. In special circumstances, the arcs of the high frequency region and the intermediate frequency region almost overlap, which increases the difficulty of clarifying the attributable electrochemical process.

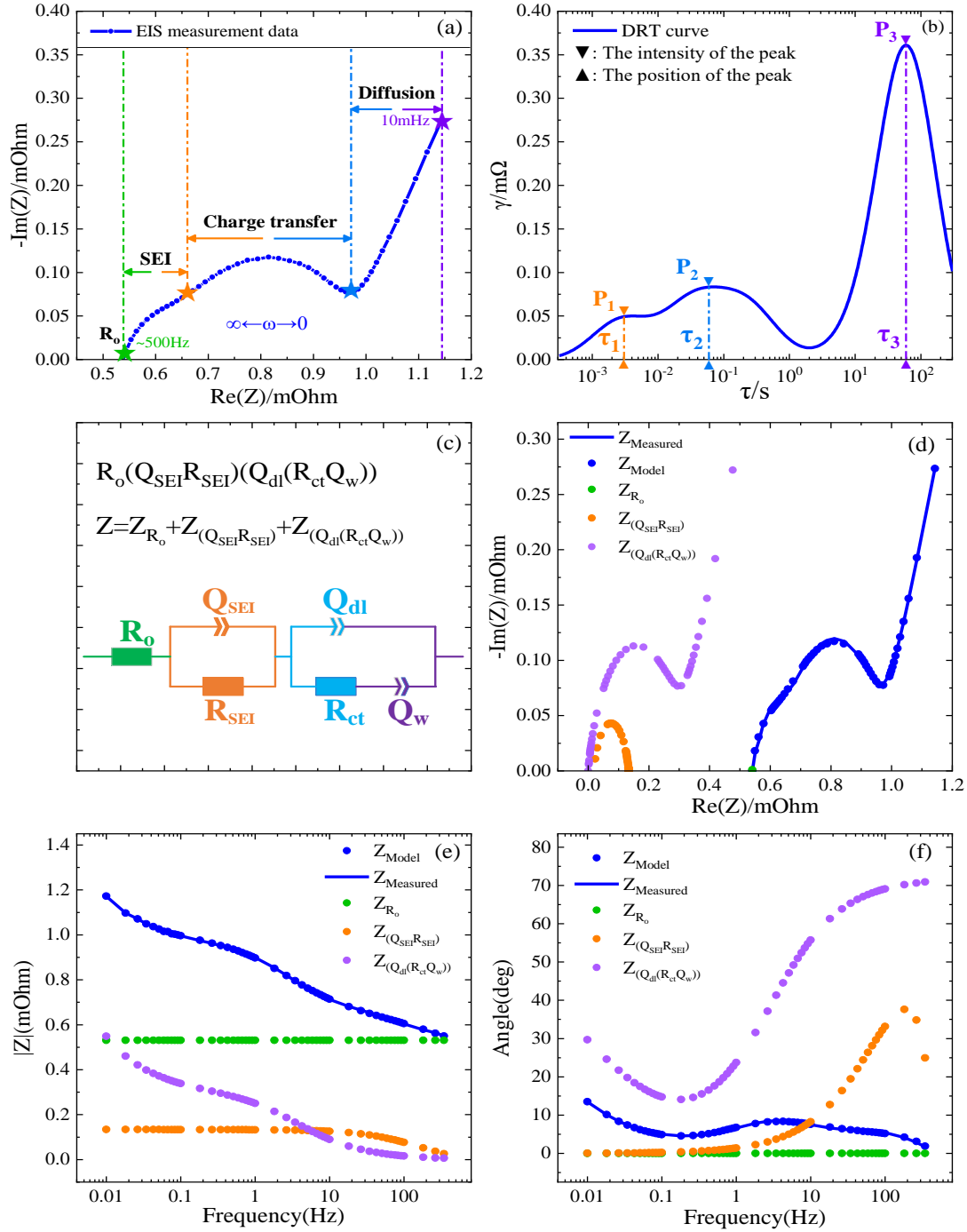


Fig. 5. The impedance spectrum test result of a typical lithium-ion battery (a) The Nyquist plot of the impedance spectrum (b) The DRT curve of the impedance spectrum (c) The ECM with the fixed circuit structure determined by the DRT method (d) The Nyquist diagram of partial and whole impedance (e) The amplitude-frequency characteristic of partial and whole impedance (f)

The phase-frequency characteristic of partial and whole impedance

Essentially, capacitive reactance arc is a relaxation process in which a capacitor is charged and discharged through a resistor after being disturbed by a weak sinusoidal

alternating current. The speed of the relaxation process is usually characterized by the time constant τ , and affects the frequency range of the capacitive reactance arc. The DRT method based on radial basis function and regularized regression can effectively separate the relaxation process in EIS and determine the time constants for each part of the impedance [34]. It regards the EIS of the battery as a circuit composed of an ohmic internal resistance R_o and an infinite number of RC parallel branches with different time constants in series, and expresses the RC parallel branches through radial basis function discretization. Meanwhile, the discretization parameters are calculated with regularized regression, and then DRT parameters are obtained by fitting the measured impedance (Z_{Mea}). The expression of DRT impedance (Z_{DRT}) is as follows:

$$Z_{DRT} = R_o + \int_{-\infty}^{\infty} \frac{\gamma(\ln \tau)}{1 + jW\tau} d \ln \tau \quad (6)$$

$\gamma(\ln \tau)$ is a DRT function composed of N radial basis functions with central characteristic time τ_n and shape factor μ , The discretized expression is written as follows:

$$\gamma(\ln \tau) = \sum_{n=1}^N x_n e^{-(\mu(\ln \tau - \ln \tau_n))^2} \quad (7)$$

x_n is the parameter to be identified, which is determined by fitting the measured electrochemical impedance spectrum. The sum of squares of errors between the fitted value and the measured value is used as the basic cost function, and the square of the first derivative of the DRT function is added to the cost function as a penalty term. It is aimed to solve the existing ill-conditioned problems through regularization methods. Thereby the cost function is determined as:

$$\min \sum_{w=w_{min}}^{w_{max}} \left[\alpha \text{Re}(Z_{Mea}(w) - Z_{DRT}(x, w))^2 + \beta \text{Im}(Z_{Mea}(w) - Z_{DRT}(x, w))^2 + \lambda \frac{d\gamma(\ln \tau)^2}{d \ln \tau} \right] \quad (8)$$

α and β are weighting factors, Re and Im are functions of the real and imaginary parts of the impedance. λ is a regularization parameter, and the optimal value is searched by regression algorithm [35, 36]. The approximation method based on the radial basis function has the advantages of fast convergence, no special distribution, simple and flexible implementation. Eventually, the specific relationship between τ and

$\gamma(\ln \tau)$ is confirmed, and the DRT curve of the typical lithium-ion battery is drawn in Fig. 5(b). It is composed of three obvious peaks, representing the SEI, charge transfer and diffusion process in EIS, respectively. Markedly, P_i is the intensity of the i -th ($i=1,2,3$) peak, and τ_i is the position, that is, the time constant of the relaxation process. Therefore, the feature parameter set θ_{DRT} that can be extracted.

$$\theta_{DRT} = \{P_1, P_2, P_3, \tau_1, \tau_2, \tau_3, P_3 - P_2, P_2 - P_1, P_3 - P_1, \tau_3 - \tau_2, \tau_2 - \tau_1, \tau_3 - \tau_1\} \quad (9)$$

The parameter set θ_{DRT} only contains the time constant information of each process in the impedance spectrum. To obtain more abundant and detailed dynamic characteristic parameters, the ECM is constructed, with the fixed circuit structure determined by the DRT method, as depicted in Fig. 5(c). R_o 、 R_{SEI} 、 R_{ct} are the ohmic impedance, SEI film resistance and charge transfer resistance, respectively. Due to the inhomogeneity of the electrode/electrolyte interface, the arc in Fig. 5(a) is not an ideal semicircular trajectory, which is generally called the "dispersion effect". Hence, the constant phase element (CPE) with capacitive nature is introduced, and is denoted by Q . The capacitance of the SEI film and the electric double layer can be represented by Q_{SEI} and Q_{dl} . Similarly, the approximate low-frequency straight line is considered to be an arc with an infinite radius, so that the diffusion impedance of the solid phase can also be expressed as Q_w . The circuit description code (CDC) of the model is $R_o(Q_{SEI}R_{SEI})(Q_{dl}(R_{ct}Q_w))$, and the total impedance Z_{Mod} and the impedance of each part are expressed as:

$$Z_{Mod} = Z_{R_o} + Z_{(Q_{SEI}R_{SEI})} + Z_{(Q_{dl}(R_{ct}Q_w))} \quad (10)$$

$$Z_{R_o} = R_o \quad (11)$$

$$Z_{(Q_{SEI}R_{SEI})} = \frac{R_{SEI}}{(j\omega)^{n_{SEI}} * Q_{SEI} * R_{SEI} + 1} \quad (12)$$

$$Z_{(Q_{dl}(R_{ct}Q_w))} = \frac{R_{ct} + (j\omega)^{n_w} * Q_w}{(j\omega)^{n_{dl}} * Q_{dl} * (R_{ct} + (j\omega)^{n_w} * Q_w) + 1} \quad (13)$$

In the above formulas, n is the order of the CPE. It is an empirical constant that is often used to modify the capacitance when fitting the impedance spectrum. The PSO algorithm is executed to effectively identify the parameters of the model, and the optimization goal is to minimize the RMSE between Z_{Mod} and Z_{Mea} . To avoid the over-fitting phenomenon caused by the complicated model parameters, n_{SEI} and n_{dl} are

fixed to 0.8 according to [37-39] and the statistical results of the identification parameters. Accordingly, the model parameter set θ_{Mod} to be identified and the optimization goal are as follows:

$$\min_{\theta_{Mod}} \sum_{w=w_{min}}^{w_{max}} (Z_{Mea}(w) - Z_{Mod}(w, \theta_{Mod}))^2 \quad (14)$$

$$\theta_{Mod} = \{R_o, R_{SEI}, R_{ct}, Q_{SEI}, Q_{dl}, Q_w, n_w\} \quad (15)$$

Perform the proposed dynamic characteristic analysis method, and the RMSE of all the measured batteries does not exceed 4×10^{-6} Ohm. To comprehensively evaluate the fitting effect and explore the contribution of each part to the total impedance, the Nyquist diagram and Bode plot of partial and whole impedance are displayed in Fig. 5(d, e, f). From the perspective of the fitting effect, regardless of the Nyquist diagram or the Bode plot, the measured value and the fitted value are highly coincident. Comparing the contribution of each part to the total impedance in the amplitude-frequency characteristic, as shown in Fig. 5(e), R_o is a constant value in the whole frequency range. Without considering R_o , the impedance of $(Q_{SEI}R_{SEI})$ in the middle-high frequency segment dominates. On the contrary, as the frequency decreases, the impedance of $(Q_{SEI}R_{SEI})$ tends to stabilize, and is exceeded by the impedance of $(Q_{dl}(R_{ct}Q_w))$. In the entire impedance spectrum, each component is aliased, which is difficult to distinguish independently. Through model parameter identification and separate calculation, the proportion of each part of the impedance in different frequency ranges can be effectively confirmed.

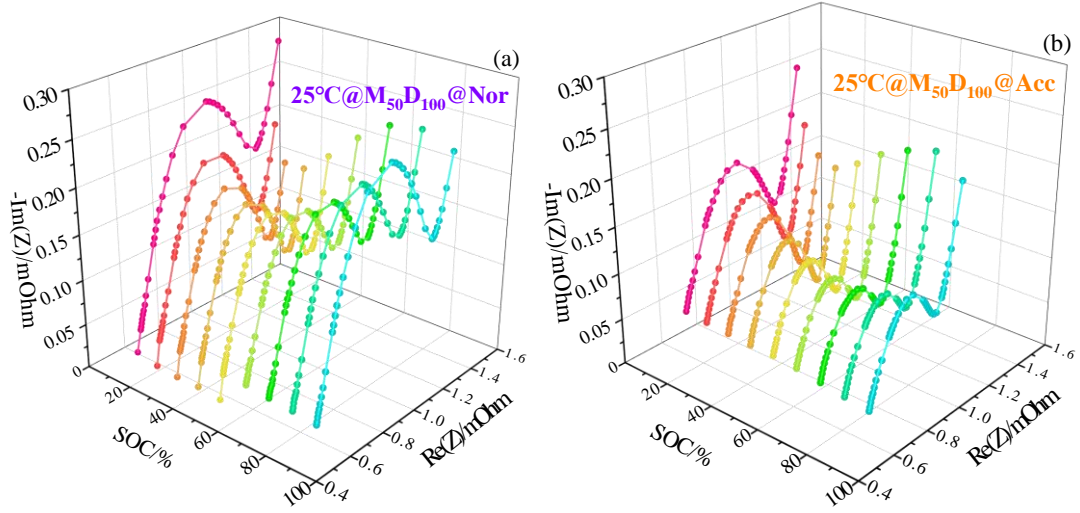


Fig. 6. The Nyquist diagram of aged battery at different SOC (a) The Nyquist diagram of battery at the condition of 25°C@M₅₀D₁₀₀@Nor (b) The Nyquist diagram of battery at the condition of 25°C@M₅₀D₁₀₀@Acc

The impedance characteristic of the battery is not only extremely related to the frequency range, but also strongly dependent on the SOC state of the battery due to the difference in the lithium insertion rate of the positive and negative materials. Taking the conditions of 25°C@M₅₀D₁₀₀@Acc and 25°C@M₅₀D₁₀₀@Nor as examples, the Nyquist diagrams of them at different SOC are shown in Fig. 6(a, b). It can be clearly observed that no matter whether the battery performance is accelerated decay or normal aging, the impedance varies with the SOC, and the degree of variation is also diverse. To in-depth explore the impedance characteristics after accelerated degradation of battery performance, the θ_{DRT} and θ_{Mod} at different SOC can be utilized. They are uniformly characterized in the form of the change rate θ^{CR} , since the EFC and the state of health after battery aging are inconsistent.

$$\theta^{CR} = \frac{\theta_{age} - \theta_{new}}{EFC}, \theta_{age}, \theta_{new} \in \{\theta_{DRT}, \theta_{Mod}\} \quad (16)$$

θ_{new} and θ_{age} are the characteristic parameters corresponding to the new and aging state of the battery, respectively, which are belong to the θ_{DRT} and θ_{Mod} . The evolution of all parameters in θ^{CR} is statistically analyzed, and the dynamic characteristic parameter θ_{DCP} that is strongly associated with the battery performance mutation can be summarized.

$$\theta_{DCP} = \{\tau_2^{CR}, (\tau_3 - \tau_2)^{CR}, R_{ct}^{CR}, Q_w^{CR}\} \quad (17)$$

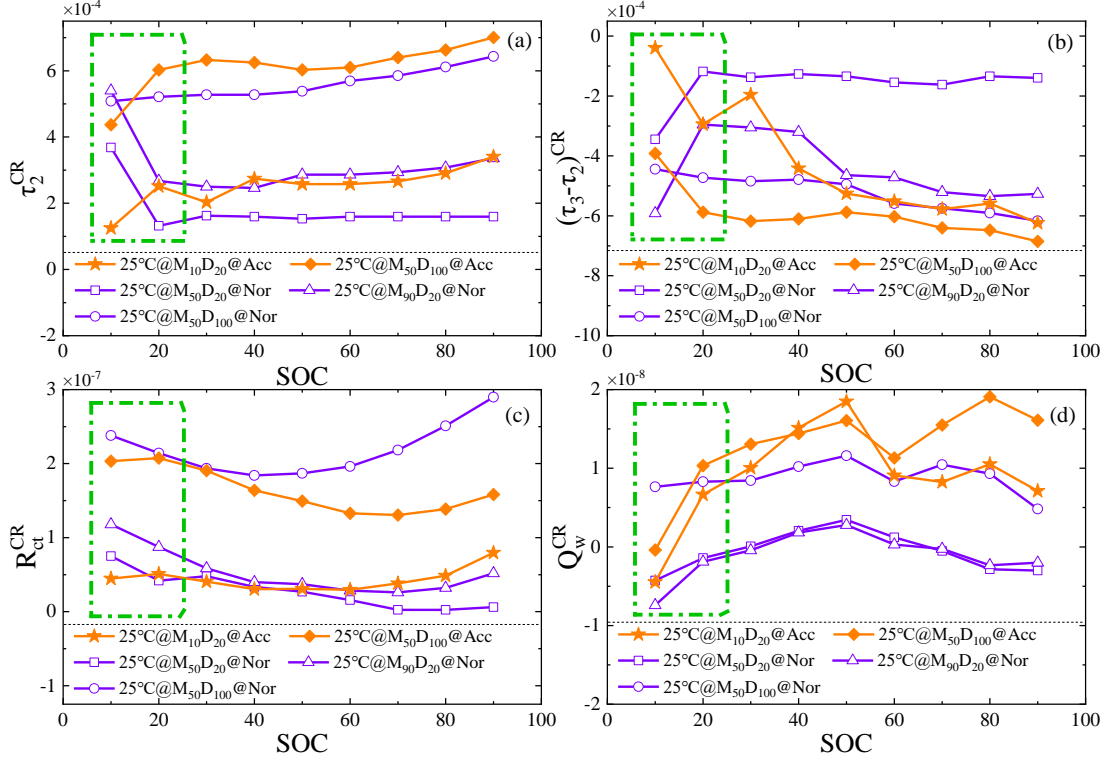


Fig. 7. The variation curves of dynamic characteristic parameter under different SOC interval cycle conditions (a) The variation curves of τ_2^{CR} under different SOC interval cycle conditions (b) The variation curves of $(\tau_3 - \tau_2)^{CR}$ under different SOC interval cycle conditions (c) The variation curves of R_{ct}^{CR} under different SOC interval cycle conditions (d) The variation curves of Q_w^{CR} under different SOC interval cycle conditions

It is exciting to indicate the battery performance mutation through the variation of battery impedance parameter at different SOC. Fig. 7 demonstrates the variation curves of each parameter in θ_{DCP} with SOC under different SOC interval cycle conditions. Focusing on the low SOC area of 10%-20% (the green dotted line area in Fig. 7), the mutant battery and the normal battery are differentiated from each other. For the mutant batteries (the orange lines in Fig. 7), when the SOC changes from 10% to 20%, τ_2^{CR} and Q_w^{CR} increase significantly, R_{ct}^{CR} slightly increases, and $(\tau_3 - \tau_2)^{CR}$ presents a significant downward trend. Conversely, τ_2^{CR} significantly decreases or slightly increases, $(\tau_3 - \tau_2)^{CR}$ significantly increases or slightly decreases, R_{ct}^{CR} decreases significantly, and Q_w^{CR} slightly increases for normal batteries, as the purple lines shown in Fig. 7. More specifically, for the normal batteries that cycled in partial SOC interval, τ_2^{CR} significantly decreases, and $(\tau_3 - \tau_2)^{CR}$ significantly increases. However, τ_2^{CR}

slightly increases, and $(\tau_3 - \tau_2)^{CR}$ slightly decreases for the normal batteries that cycled in entire SOC interval. In view of this, the diverse exhibition of θ_{DCP} at the low SOC not only facilitates the accurate identification of battery performance mutation, but also promotes the judgment of battery aging path.

Similar behavior can be deduced under different temperature cycle conditions, as proved in Fig. 8. It is worth noting that when the SOC is changed from 10% to 20% (the green dotted line area in Fig. 8), for the case of 35°C@M₅₀D₁₀₀@Nor, the change tendency of Q_w^{CR} is consistent with the mutant battery, as the square line shown in Fig. 8(d). Thus, there may be a risk of lapse in identifying a mutant battery with only single parameter. As shown in Fig. 8(a, b, c), if other parameters that have obvious distinction between normal and mutation are combined, such as τ_2^{CR} , $(\tau_3 - \tau_2)^{CR}$, or R_{ct}^{CR} , the accuracy will be ensured. In addition, the parameter difference between the temperature cycle conditions of normal batteries also exists. Especially, when the temperature reaches 45 °C and 55 °C, in the SOC range of 10%-20%, τ_2^{CR} and $(\tau_3 - \tau_2)^{CR}$ exhibit the opposite trends compared to 25 °C and 35 °C.

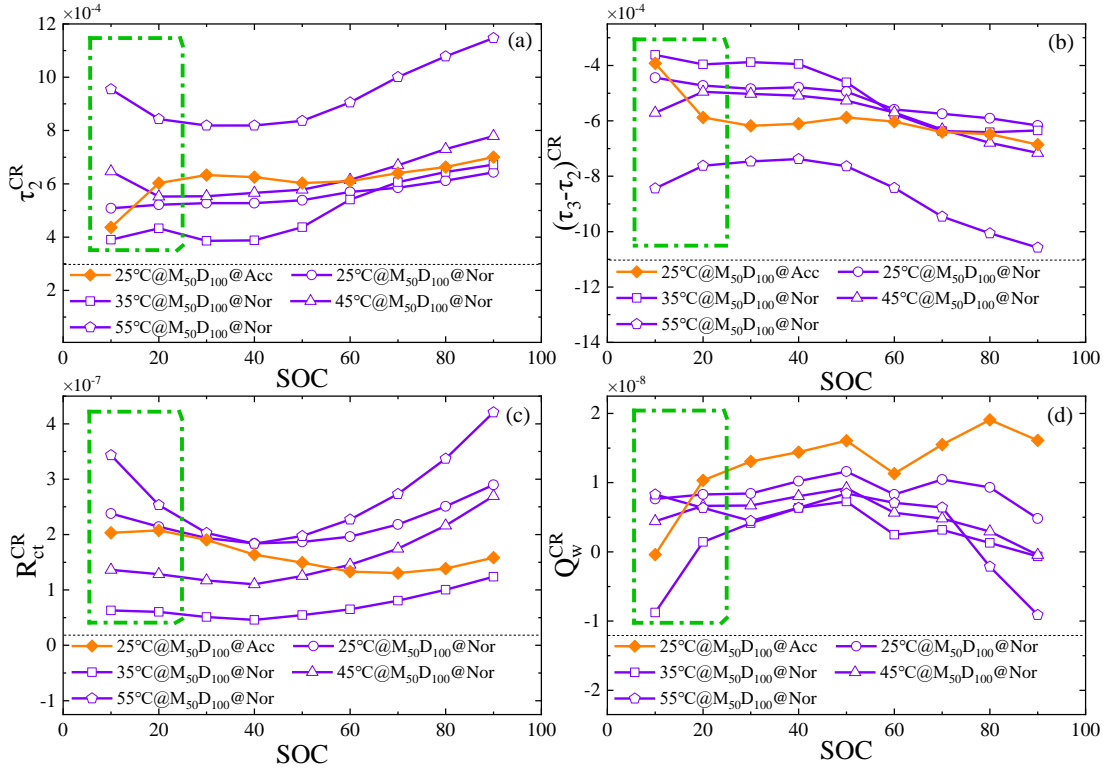


Fig. 8. The variation curves of dynamic characteristic parameter under different temperature cycle conditions (a) The variation curves of τ_2^{CR} under different temperature cycle conditions (b) The

variation curves of $(\tau_3 - \tau_2)^{CR}$ under different temperature cycle conditions (c) The variation curves of R_{ct}^{CR} under different temperature cycle conditions (d) The variation curves of Q_w^{CR} under different temperature cycle conditions

The analysis results of temperature and SOC operating conditions further demonstrate the feasibility of identifying mutant battery and aging path based on the proposed parameter set. It can be seen that the prospect of impedance-based battery aging and abnormal state diagnosis is brilliant. Considering the physical meaning of θ_{DCP} , the performance mutation is mainly reflected in the abnormal charge transfer and diffusion process, and it is concentrated in the low SOC region of 10%-20%. Coincidentally, this region is embraced in the cyclic SOC interval where the performance mutation occurs. It can be concluded that the SOC cycle interval has an essential influence on the process of battery performance degradation, especially the low SOC interval, which is more liable to engender mutation. A blessing in disguise is that the charge transfer impedance and diffusion impedance in this SOC interval are more sensitive to mutation. With this feature, the effect of identifying performance mutation is excellent.

4 Conclusion

The performance mutation effect under different cyclic conditions has been studied. The thermodynamic investigation method based on the half-cell potential synthesis and the dynamic investigation method based on DRT and ECM are implemented. In addition, the equilibrium potential and impedance characteristics that determine the external performance of battery are explored. This research has proposed the mechanism of battery performance mutation and summarized as follows:

- 1) Experiments have confirmed that under normal temperature conditions, whether cycling within full or partial SOC range, the battery is very likely experience performance mutation. Furthermore, the cyclic interval of low SOC is more liable to engender mutation. However, elevated temperature is not the dominant factor that causes the performance mutation.

2) Mutation mechanism and parameterized characterization based on equilibrium potential are investigated. The mutation effect containing inducing point and crossing point is caused by the mutation of the negative active material. Moreover, the necessary and sufficient conditions for the occurrence of mutations are derived, and the thermodynamic characteristic parameters are extracted.

3) Mutation mechanism and parameterized characterization based on impedance features are explored. The charge transfer impedance and diffusion impedance in the low SOC range are particularly sensitive to the mutation. And the dynamic parameters that characterize the mutation are proposed.

The mutation mechanism of the battery and related extracted parameters have been proposed, providing the foundation for battery performance mutation diagnosis and prognosis. The online acquisition method of the parameters still needs further investigated.

5 Acknowledgment

This work was supported by the Natural Science Foundation of Beijing Municipality [No. 3212033]; National Natural Science Foundation of China [No. 51977007, No. 52007006]; and the Fundamental Research Funds for the Central Universities [2020JBZD012].

6 References:

- [1] Andwari Am, Pesiridis A, Rajoo S, et al., A review of Battery Electric Vehicle technology and readiness levels[J]. 2017. 78: 414-430.
- [2] Barre A, Deguilhem B, Grolleau S, et al., A review on lithium-ion battery ageing mechanisms and estimations for automotive applications[J]. 2013. 241: 680-689.
- [3] Zhu J, Wierzbicki T, Li W, A review of safety-focused mechanical modeling of commercial lithium-ion batteries[J]. 2018. 378: 153-168.
- [4] Kabir Mm, Demirocak Dervisemre, Degradation mechanisms in Li-ion batteries: a state-of-the-art review[J]. 2017(6).
- [5] Zhang Caiping, Wang Yubin, Gao Yang, et al., Accelerated fading recognition for lithium-ion batteries with Nickel-Cobalt-Manganese cathode using quantile regression method[J]. Applied Energy, 2019. 256: 113841.
- [6] Klett M, Eriksson R, Groot J, et al., Non-uniform aging of cycled commercial LiFePO₄//graphite cylindrical cells revealed by post-mortem analysis[J]. 2014. 257: 126-137.

- [7] Bacha Tobiasc, Schusterb Simonf, Fledera Elena, et al., Nonlinear aging of cylindrical lithium ion cells linked to heterogeneous compression[J]. 2016. 5: 212-223.
- [8] Ma Xw, Harlow Je, Li J, et al., Hindering Rollover Failure of Li[Ni_{0.5}Mn_{0.3}Co_{0.2}]O₂/Graphite Pouch Cells during Long-Term Cycling[J]. 2019. 166(4): A711-A724.
- [9] Sarasketa-Zabala E, Aguesse F, Villarreal I, et al., Understanding Lithium Inventory Loss and Sudden Performance Fade in Cylindrical Cells during Cycling with Deep-Discharge Steps[J]. 2015. 119(2): 896-906.
- [10] Klett Matilda, Svens Pontus, Tengstedt Carl, et al., Uneven Film Formation across Depth of Porous Graphite Electrodes in Cycled Commercial Li-Ion Batteries[J]. Journal of Physical Chemistry C, 2015. 119(1): 90-100.
- [11] Zier Martin, Scheiba Frieder, Oswald Steffen, et al., Lithium dendrite and solid electrolyte interphase investigation using OsO₄[J]. Journal of Power Sources, 2014. 266: 198-207.
- [12] Ecker Madeleine, Shafiei Sabet Pouyan, Sauer Dirkuwe, Influence of operational condition on lithium plating for commercial lithium-ion batteries – Electrochemical experiments and post-mortem-analysis[J]. Applied Energy, 2017. 206: 934-946.
- [13] Yang Xiao-guang, Wang Chao-yang, Understanding the trilemma of fast charging, energy density and cycle life of lithium-ion batteries[J]. Journal of Power Sources, 2018. 402: 489-498.
- [14] Zhang Lj, Mu Zq, Sun Cy, Remaining Useful Life Prediction for Lithium-Ion Batteries Based on Exponential Model and Particle Filter[J]. IEEE Access, 2018. 6: 17729-17740.
- [15] Guha Arijit, Patra Amit, State of Health Estimation of Lithium-Ion Batteries Using Capacity Fade and Internal Resistance Growth Models[J]. IEEE Transactions on Transportation Electrification, 2018. 4(1): 135-146.
- [16] Xue Zhiwei, Zhang Yong, Cheng Cheng, et al., Remaining useful life prediction of lithium-ion batteries with adaptive unscented kalman filter and optimized support vector regression[J]. Neurocomputing, 2020. 376: 95-102.
- [17] Sarasketa-Zabala E, Gandiaga I, Martinez-Laserna E, et al., Cycle ageing analysis of a LiFePO₄/graphite cell with dynamic model validations: Towards realistic lifetime predictions[J]. Journal of Power Sources, 2015. 275: 573-587.
- [18] Zhang Qi, Shang Yunlong, Li Yan, et al., A novel fractional variable-order equivalent circuit model and parameter identification of electric vehicle Li-ion batteries[J]. ISA Transactions, 2020. 97: 448-457.
- [19] Ma Zeyu, Yang Ruixin, Wang Zhenpo, A novel data-model fusion state-of-health estimation approach for lithium-ion batteries[J]. Applied Energy, 2019. 237: 836-847.
- [20] Gao Peng, Zhang Cuifen, Wen Guangwu, Equivalent circuit model analysis on electrochemical impedance spectroscopy of lithium metal batteries[J]. Journal of Power Sources, 2015. 294: 67-74.
- [21] Andre D, Meiler M, Steiner K, et al., Characterization of high-power lithium-ion batteries by electrochemical impedance spectroscopy. II: Modelling[J]. Journal of Power Sources, 2011. 196(12): 5349-5356.
- [22] Zhou Xing, Huang Jun, Pan Zhengqiang, et al., Impedance characterization of lithium-ion batteries aging under high-temperature cycling: Importance of electrolyte-phase diffusion[J]. Journal of Power Sources, 2019. 426: 216-222.
- [23] Fu Rujian, Choe Song-yul, Agubra Victor, et al., Development of a physics-based degradation model for lithium ion polymer batteries considering side reactions[J]. Journal of Power Sources, 2015. 278: 506-521.
- [24] Jin Xing, Vora Ashish, Hoshing Vaidehi, et al., Physically-based reduced-order capacity loss model

- for graphite anodes in Li-ion battery cells[J]. *Journal of Power Sources*, 2017. 342: 750-761.
- [25] Pinson Mb, Bazant Mz, Theory of SEI Formation in Rechargeable Batteries: Capacity Fade, Accelerated Aging and Lifetime Prediction[J]. *Journal of the Electrochemical Society*, 2012. 160(2): A243-A250.
- [26] Yang Xg, Leng Yj, Zhang Gs, et al., Modeling of lithium plating induced aging of lithium-ion batteries: Transition from linear to nonlinear aging[J]. 2017. 360: 28-40.
- [27] Maheshwari Arpit, Heck Michael, Santarelli Massimo, Cycle aging studies of lithium nickel manganese cobalt oxide-based batteries using electrochemical impedance spectroscopy[J]. *Electrochimica Acta*, 2018. 273: 335-348.
- [28] Chang Yang, Fang Huajing, Zhang Yong, A new hybrid method for the prediction of the remaining useful life of a lithium-ion battery[J]. 2017. 206: 1564-1578.
- [29] Wei Jingwen, Dong Guangzhong, Chen Zonghai, Remaining Useful Life Prediction and State of Health Diagnosis for Lithium-Ion Batteries Using Particle Filter and Support Vector Regression[J]. 2018. 65(7): 5634-5643.
- [30] Cong Xinwei, Zhang Caiping, Jiang Jiuchun, et al., An Improved Unscented Particle Filter Method for Remaining Useful Life Prognostic of Lithium-ion Batteries with Li(NiMnCo)O₂ Cathode with Capacity Diving[J]. *IEEE Access*, 2020. PP(99): 1.
- [31] Dubarry Matthieu, Truchot Cyril, Liaw Boryann, Synthesize battery degradation modes via a diagnostic and prognostic model[J]. *Journal of Power Sources*, 2012. 219: 204-216.
- [32] Gao Yang, Yang Sijia, Jiang Jiuchun, et al., The Mechanism and Characterization of Accelerated Capacity Deterioration for Lithium-Ion Battery with Li(NiMnCo) O₂ Cathode[J]. *Journal of The Electrochemical Society*, 2019. 166(8): A1623-A1635.
- [33] Schönleber M, Klotz D, Ivers-Tiffée E, A Method for Improving the Robustness of linear Kramers-Kronig Validity Tests[J]. *Electrochimica Acta*, 2014. 131: 20-27.
- [34] Wan Tinghei, Saccoccio Mattia, Chen Chi, et al., Influence of the Discretization Methods on the Distribution of Relaxation Times Deconvolution: Implementing Radial Basis Functions with DRTtools[J]. *Electrochimica Acta*, 2015. 184: 483-499.
- [35] Saccoccio Mattia, Wan Tinghei, Chen Chi, et al., Optimal Regularization in Distribution of Relaxation Times applied to Electrochemical Impedance Spectroscopy: Ridge and Lasso Regression Methods - A Theoretical and Experimental Study[J]. *Electrochimica Acta*, 2014. 147: 470-482.
- [36] Shafiei Sabet Pouyan, Sauer Dirkuwe, Separation of predominant processes in electrochemical impedance spectra of lithium-ion batteries with nickel-manganese-cobalt cathodes[J]. *Journal of Power Sources*, 2019. 425: 121-129.
- [37] Attidekou Pierrots, Lambert Simon, Armstrong Matthew, et al., A study of 40 Ah lithium ion batteries at zero percent state of charge as a function of temperature[J]. *Journal of Power Sources*, 2014. 269: 694-703.
- [38] Li Shengboeben, Wang Baojin, Peng Huei, et al., An electrochemistry-based impedance model for lithium-ion batteries[J]. *Journal of Power Sources*, 2014. 258: 9-18.
- [39] Tröltzsch Uwe, Kanoun Olfa, Tränkler Hans-rolf, Characterizing aging effects of lithium ion batteries by impedance spectroscopy[J]. *Electrochimica Acta*, 2006. 51(8-9): 1664-1672.